Journal of Metals, Materials and Minerals, 36(2), e2386, 2026

Fabrication of a chitosan–Fe_3O_4/activated carbon/TiO_2 nanocomposite as a Pb(II) heavy metal adsorbent

Berliantty Warim PUTRI[1], Arif HIDAYAT[1], Lya Rizka HERAWATI[1], Poppy PUSPITASARI[2], Nandang MUFTI[1], Yap Wing FEN[3,4], Muhammad Safwan Abdul AZIZ[5], Tahta AMRILLAH[6], Ahmad TAUFIQ[1,*]

[1] *Department of Physics, Faculty of Mathematics and Natural Sciences, Universitas Negeri Malang, Jl. Semarang 5 Malang 65145, Indonesia*
[2] *Department of Mechanical Engineering, Faculty of Engineering, Universitas Negeri Malang, Jl. Semarang 5, Malang 65145, Indonesia*
[3] *Department of Physics, Faculty of Science, Universiti Putra Malaysia, 43400 UPM Serdang, Selangor, Malaysia*
[4] *Functional Nanotechnology Devices Laboratory, Institute of Nanoscience and Nanotechnology, Universiti Putra Malaysia, 43400 UPM Serdang, Selangor, Malaysia*
[5] *Department of Physics, Faculty of Science, Universiti Teknologi Malaysia, Johor Bahru, Malaysia*
[6] *Nanotechnology Engineering, Faculty of Advanced Technology and Multidiscipline, Universitas Airlangga, Indonesia*

***Corresponding author e-mail**: ahmad.taufiq.fmipa@um.ac.id

Received date:
29 April 2025
Revised date:
19 August 2025
Accepted date:
26 December 2025

Keywords:
CS–Fe_3O_4/AC/TiO_2;
Absorbent;
Heavy metal;
Superparamagnetism;
Industrial waste

Abstract

Nowadays, water pollution by heavy metal Pb(II) is a significant issue in many countries, including Indonesia. To overcome this problem, a suitable and efficient waste treatment method is necessary. Therefore, in this work, Fe_3O_4/AC/TiO_2 nanocomposite modified with chitosan (CS) for the treatment of Pb (II) waste were investigated. CS was used due to its OH and NH_2 functional groups, which enable the formation of a new hybrid nanocomposite that can be used repeatedly. To reduce production costs, environmentally friendly, raw natural materials, such as iron sand, coconut shells, and shrimp shells, were employed. The XRD characterization results indicate that the crystallite size of Fe_3O_4 is in the range of 16.05 nm to 24.52 nm, while that of TiO_2 is 25.22 nm. The SEM–EDX characterization indicates that the particle morphology is imperfectly round and aggregated. Furthermore, the FTIR analysis indicates the presence of N–H, Fe–O, C=O, and Ti–O–Ti functional groups, representing the CS, Fe_3O_4, AC, and TiO_2 characteristics. The VSM results demonstrate that the CS-Fe_3O_4/AC/TiO_2 exhibits superparamagnetic properties. In the Pb (II) heavy metal uptake test, CFAT 1 showed the most optimal results when the adsorption test was conducted for 120 min, resulting in an efficiency of 99.88%. Furthermore, this sample can be used repeatedly in four adsorption-desorption cycles. This suggests that the CS–Fe_3O_4/AC/TiO_2 nanocomposite can be an effective Pb(II) heavy metal absorbent.

1. Introduction

Water is a vital resource for all living organisms that is essential for survival [1]. However, a significant number of industries dispose of waste in rivers in an unregulated and careless manner, resulting in the contamination of water sources with a range of heavy metals, including Pb, Cd, Ni, Cu, Cr, and Hg [2,3]. Furthermore, among these heavy metals, Pb is reflected to be the most toxic contaminant [4-5]. The World Health Organization (WHO) has recognized the adverse effects of Pb contamination on the reproduction, nervous system, kidneys, and liver [6]. Furthermore, Pb contamination is generated by waste from the battery and car manufacturing industries [7,8], batik production [9], mining [10], and others.

A heavy metal content investigation at a gold mine in Pongkor, Indonesia, exposed the presence of Pb with a concentration of 71.55 ppm [11]. This concentration is far above the wastewater quality standard, which is 0.01 ppm for Pb(II) metal ions [12]. Subsequently, a specific strategy is necessary to solve the problem of wastewater pollution. So far, numerous strategies and methods have been developed, including irradiation, coagulation, filtration, oxidation, and precipitation, as well as aerobic and anaerobic processes. Conversely, these methods have limitations such as high costs, ineffectiveness, complex mechanisms, and inefficiency [13]. Among these methods, the adsorption method is believed to be the most effective and widely used to mitigate waste-water pollution. This method offers a safe and straightforward process that does not involve expensive costs [14]. Hence, this work explores nanocomposite-based adsorbents to eliminate heavy metals from wastewater. Theoretically, the nanocomposite adsorption capacity is dependent on the particle size, with a greater capacity for a smaller particle size [15]. Consequently, applications related to the interaction of nanomaterials with the environment rely heavily on their surface functionality, necessitating materials that are chemically stable, uniform in size, and well-dispersible in liquid media.

One material that can be added as an adsorbent is the Fe_3O_4 nano-particle. At the nanoscale, Fe_3O_4 exhibits superramagnetic propertied and facile recycling [16]. These nanoparticles are exceptionally effective for removing heavy metal ions. Unfortunately, this material readily forms agglomerates in liquid and experiences oxidation, necessitating

modifications to prevent agglomeration [17-19]. This problem can be overcome by combining it with other materials, such as TiO_2, which is chemically and biologically inert and nontoxic. However, its relatively low adsorption capacity necessitates its modification with porous substances, such as a carbon-based material [20]. In this study, activated carbon (AC) was selected for its extensive surface area, porous structure, substantial reactive surface area, and high adsorption capacity, which collectively enhance the adsorption capacity for heavy metals [21]. In previous studies, the synthesis of $Mg_{0.2}Fe_{2.8}O_4$/AC/TiO_2 nanocomposite adsorbents was successfully achieved using the coprecipitation method, resulting in the highest adsorbent efficiency value, reaching 99.90%, at a contact time of 30 min for lead metal (Pb). However, a notable drawback of this adsorbent is its lack of reusability due to the use of acidic materials that damage the materials [22]. Based on this phenomenon, it is important to modify the surface of the nanocomposite with compatible functional groups [23].

In the present study, chitosan (CS) was introduced to increase the adsorption performance of a combination of Fe_3O_4, AC, and TiO_2, forming CS–Fe_3O_4/AC/TiO_2 nanocomposite. CS was selected because it has suitable chemical functional groups that support adsorbents, such as amine (NH_2) and hydroxyl (OH) [24]. Such functional groups are able to interact with heavy metal ions and retain them even after the desorption process with acidic materials [25]. The CS functional groups are considered to allow Fe_3O_4/AC/TiO_2 nanocomposite to be used repeatedly. In line with this explanation, a previous study showed that the addition of CS to several adsorbents led to excellent regeneration and recycling due to the presence of carboxymethyl groups [24]. Interestingly, to reduce production costs, this work employed some natural materials as precursors, such as iron sand to produce Fe_3O_4, coconut shell to produce AC, and shrimp shells to produce CS. Due to their environmentally friendly and economical nature, as well as their abundance in Indonesia, iron sand, coconut shells, and shrimp shells were selected as main precursors [26].

2. Research method

2.1 Synthesis of Fe_3O_4 nanoparticles

The materials used in this experiment were natural iron sand, coconut shell waste, shrimp shell chitosan (pharmaceutical grade with 98% purity), citric acid monohydrate (Merck), titanium chloride ($TiCl_3$, Merck), nitric acid (HNO_3, 65%, Merck), lead(II) nitrate ($Pb(NO_3)_2$, Merck), ethanol (Merck), hydrochloric acid (HCl 38%, Merck), ammonium hydroxide (NH_4OH, 25%, Merck), sodium hydroxide (NaOH, Merck), and distilled water. The Fe_3O_4 nanoparticle was synthesized through the coprecipitation method, following procedures previously described and illustrated in Figure 1 [27]. The iron sand was washed with distilled water and dried under the sun. The dried iron sand was extracted using a permanent magnet to separate impurities from the iron. This process yielded iron sand powder with 99.5% purity. The prepared iron sand (20 g) was dissolved in HCl (58 mL) and stirred for 20 min using a magnetic stirrer to produce $FeCl_2$ and $FeCl_3$ solutions. Finally, the solutions were titrated with NH_4OH, followed by a stirring process at ambient temperature for 30 min to form a black magnetite (Fe_3O_4) nanoparticle precipitate and then washed until a neutral pH was achieved. To obtain Fe_3O_4 nanoparticle powders, the final product was filtered using a filter paper and then dried at 100°C for 1 h.

2.2 Synthesis of TiO_2 nanoparticles

In this study, the coprecipitation method was employed to produce TiO_2 nanoparticles following the previous work [28]. An amount of 5 mL of $TiCl_3$ was dissolved in 15 mL of distilled water and 5 mL of HCl by stirring process using a hotplate magnetic stirrer for 1 h at 720 rpm at room temperature to obtain the $TiCl_3$ solution. Subsequently, the NH_4OH was added to the $TiCl_3$ solution and stirred for 1 h to form TiO_2 precipitates. The product was washed and filtered for the drying cycle at 100°C for 1 h. Finally, the final product was dried for 1 h at 600°C to produce TiO_2 nanoparticles. The synthesis process is illustrated in Figure 2.

2.3 Synthesis of activated carbon (AC)

The synthesis of AC was conducted by employing the carbonization method followed by chemical–physical activation [26]. The raw materials were prepared first. The coconut shells were burned to charcoal and then pulverized using a blender. Next, the charcoal was sieved using a 200 mesh sieve to get a smaller and consistent particle size. After that, the coconut shell charcoal was activated by heating in a furnace at 400°C for 5 h and cooling to room temperature. The next functionalization was conducted to improve the dispersion of AC. AC (10 g) was dissolved in 100 mL of HNO_3. The solution was stirred with a hotplate magnetic stirrer at 720 rpm for 2 h at 80°C. The sample was then washed with technical ethanol to pH 6 or pH 7. The sample was then dried and heated at 100°C for 1 h to obtain the AC powder. The entire synthesis is shown in Figure 3.

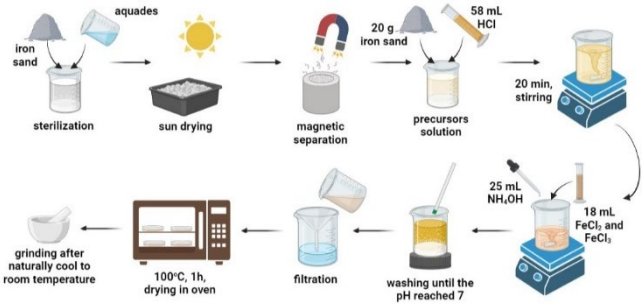

Figure 1. Synthesis of Fe_3O_4 nanoparticles.

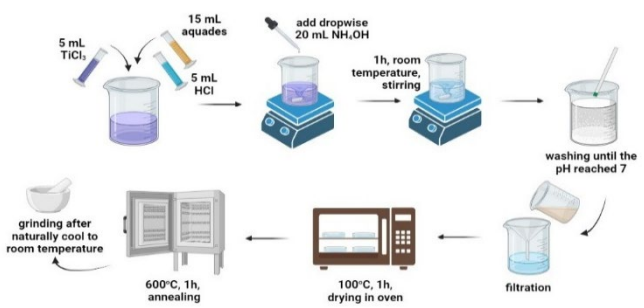

Figure 2. Synthesis of TiO_2 nanoparticles.

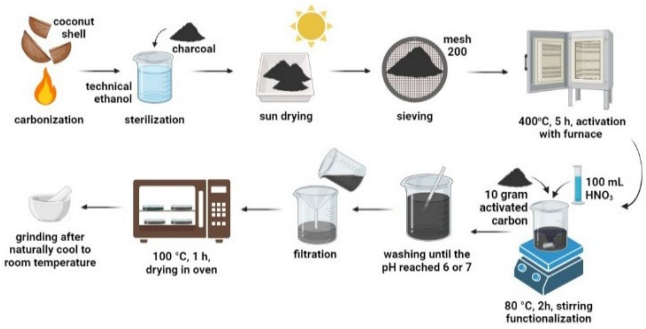

Figure 3. Synthesis of activated carbon.

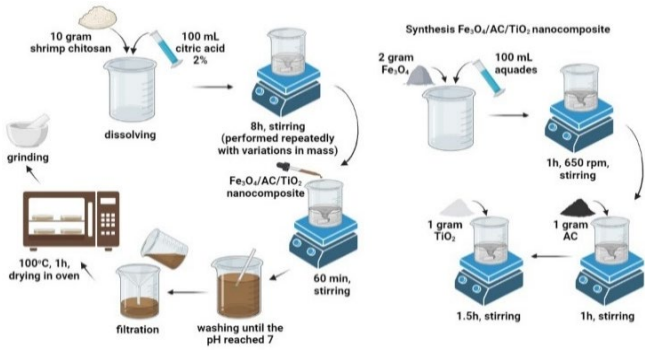

Figure 4. Synthesis of CS–Fe_3O_4/AC/TiO_2 nanocomposite.

2.4 Synthesis of CS–Fe_3O_4/AC/TiO_2 nanocomposite

The synthesis procedure of CS–Fe_3O_4/AC/TiO_2 nanocomposite can be seen in Figure 4. The synthesis was started by dissolving CS with mass variations of 0 g, 0.25 g, 0.50 g, 0.75 g, and 1.00 g in 100 mL of 2% citric acid using a stirring process by a hot plate magnetic stirrer at 720 rpm for 8 h. The product of this step was named by solution A. Furthermore, the synthesis of Fe_3O_4/AC/TiO_2 nanocomposite was initiated by dissolving 2 g of Fe_3O_4 in 100 mL of H_2O using a hot plate magnetic stirrer at 650 rpm for 1 h. To obtain the Fe_3O_4/AC composite, 1 g of AC was added to the Fe_3O_4 solution and stirred at 650 rpm for 60 min. Then, to obtain the Fe_3O_4/AC/TiO_2 nanocomposite solution (Solution B), 1 g of TiO_2 was added to the Fe_3O_4/AC solution, followed by stirring for 1.5 h at 650 rpm. Solution B was added to Solution A by titration and stirred at 720 rpm for 60 min using the ex-situ method to produce CS–Fe_3O_4/AC/TiO_2 in solution. The resulting solution was filtered using filter paper and then dried in an oven at 100°C for 1 h to form the CS–Fe_3O_4/AC/TiO_2 nanocomposite. The CS–Fe_3O_4/AC/TiO_2 nanocomposite adsorbents with CS mass variations of 0 g, 0.25 g, 0.50 g, 0.75 g, and 1.00 g were coded CFAT 1, CFAT 2, CFAT 3, CFAT 4, and CFAT 5, respectively.

2.5 Characterization

The nanocomposite of CS–Fe_3O_4/AC/TiO_2 was characterized by PANalytical X'Pert Pro x-ray diffractometry (XRD) with Cu–*Kα* X-ray radiation to identify the phase, crystal structure, and crystal size of the nanocomposite. The initial angle of the spectrum was 20° and the final angle was 80° with a step angle of 2°·min^{-1}. Phase identification was conducted by referring to the powder diffraction database obtained from the American Mineralogist Crystal Structure database (AMCSD numbers 0011765 and 0002403). Furthermore, the characterization by Fourier–transform infrared spectroscopy (FTIR; Shimadzu IR-Prestige 21) was also conducted to determine the functional groups in the nanocomposites. Characterization was performed in the wavenumber range between 4000 cm^{-1} to 400 cm^{-1}, which represents the fingerprints of molecules within the sample. Each molecule has a unique fingerprint, which is used for material identification. The surface morphology and elemental content of the nanocomposites were determined by scanning electron microscopy with energy-dispersive X-ray spectroscopy (SEM-EDX) characterization using an FEI Inspect-S50. The samples were coated with gold before characterization. The test was carried out with a high voltage of 25 kV. SEM characterization results were in the form of images equipped with a size scale. This scale was used as a reference to determine the particle size value. In addition, it also produced an EDX spectrum that can be used to confirm the elemental composition of the samples. Vibrating sample magnetometry (VSM) characterization with a PPMS® VersaLab™ Cryogen-free 3 Tesla was used to measure the magnetic properties of the nanocomposites. The result was a hysteresis curve of magnetization (*M*) with external magnetic field (*H*). Ultraviolet–visible spectroscopy (UV-Vis) spectrometer using an Analytik Jena Specord 200 plus was used to investigate the band gap energy values. Molecules containing chromophores are most sensitive to light stimuli and absorb specific wavelengths of ultraviolet or visible light. To perform a UV-Vis test on the sample, it was dissolved in deionized water to a concentration of 0.001 g·mL^{-1}. Furthermore, atomic absorption spectroscopy (AAS) characterization was also performed to determine the level of a compound element based on its atomic absorption. The sample had to be in the form of a clear solution. The AAS method was based on the absorption of light by atoms. Atoms absorb the light at certain wavelengths depending on the nature of the element. The efficiency of the nanocomposite in absorbing heavy metals in each variation was calculated using the formula in Equation (1) and Equation (2).

Adsorbent phase concentration after equilibrium, was calculated using Equation (1).

$$q_e = \left(\frac{C_i - C_e}{m}\right) V \quad (1)$$

While the percentage of metal removal (R%) is calculated by Equation (2),

$$(\text{R\% removal}) = \frac{C_i - C_e}{C_i} \times 100 \quad (2)$$

Where q_e is the adsorbent phase concentration after equilibrium (mg·g^{-1}), C_i is the initial concentration of metal ions in solution (mg·L^{-1}), C_e is the equilibrium concentration of metal ions in solution (mg·L^{-1}), V is the volume of aqueous solution (L), and m is the mass of adsorbent used (g) [29,30].

3. Results and discussion

3.1 The crystal structure of the CS–Fe_3O_4/AC/TiO_2 nanocomposite

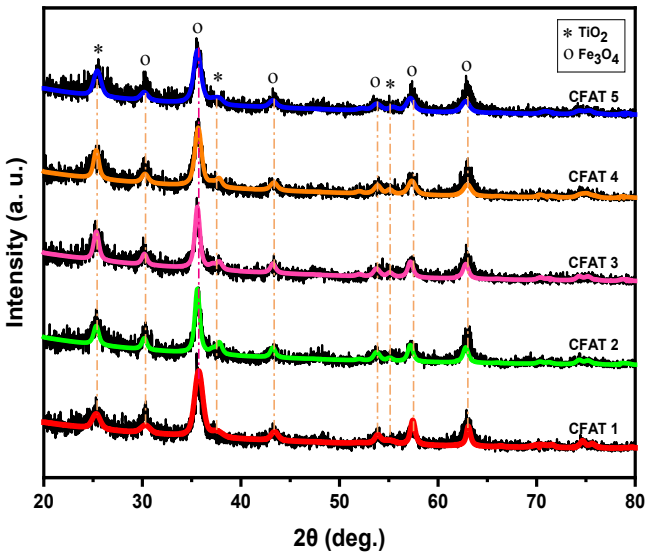

Figure 5. X-ray diffraction patterns of CFAT 1, CFAT 2, CFAT 3, CFAT 4, and CFAT 5.

Figure 5 shows the XRD diffraction pattern of the CS–Fe_3O_4/AC/TiO_2 nanocomposite (CFAT 1 to CFAT 5), where it is seen that all samples have similar patterns. The diffraction peaks detected at 2θ = 30.5°, 35.8°, 43.5°, 53.8°, 57.5°, and 63.0° that match the American Mineralogist Crystal Structure (AMCSD) 0002403 which represent a characteristics of Fe_3O_4 with hkl planes (220), (311), (400), (422), (511), and (440) with a = b = c = 8.3455 Å and cubic spinel structure [31,32]. Furthermore, there are also peaks at 2θ = 25.2°, 38.1°, and 54.0° that match the AMCSD 0011765 record for TiO_2 phase with hkl planes (110), (211), and (121). In this research, TiO_2 has lattice parameters a = b = 3.7845 Å and c = 9.5143 Å. Therefore, this diffraction pattern indicates that the crystal structures of the TiO_2 phase are rutile and anatase [28].

Moreover, for CFAT 2 to CFAT 5 samples, there are diffraction peaks of Fe_3O_4/AC/TiO_2 with the addition of CS, indicating that CS does not affect the diffraction peaks of Fe_3O_4 or TiO_2. These results are in line with the research of Liandi *et al.*, where the addition of CS did not influence the Fe_3O_4 phase [33]. In this study, no peaks from AC were observed, as AC has an amorphous structure [34]. Furthermore, the TiO_2 crystallite size in all samples was 25.22 nm, while the Fe_3O_4 crystallite size decreased as the mass of CS increased; from 24.52 nm at 0 g CS to 23.54 nm at 0.25 g, 22.07 nm at 0.5 g, 18.39 nm at 0.75 g, and 16.05 nm at 1 g, respectively. The decrease in Fe_3O_4 crystallite size as CS increases occurs as a result of the distribution of Fe_3O_4 in the CS solution, which separates the Fe_3O_4 clusters to form smaller sizes [35,36].

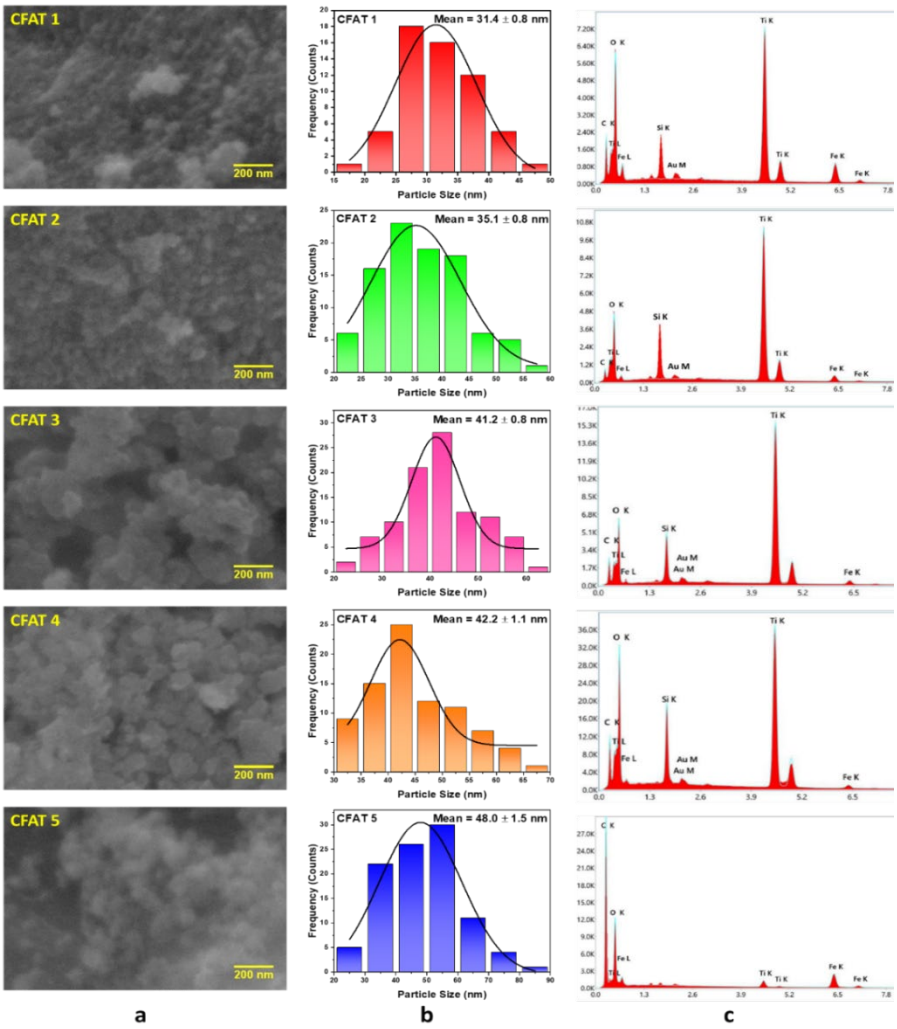

Figure 6. (a) Morphology, (b) particle size, and (c) EDX spectroscopy of CFAT 1, CFAT 2, CFAT 3, CFAT 4, and CFAT 5.

3.2 The morphology of the CS–Fe_3O_4/AC/TiO_2 nanocomposite

The morphology of the CS–Fe_3O_4/AC/TiO_2 nanocomposite is shown in Figure 6. As shown in Figure 6(a), the nanoparticles are clustered together to form agglomerations caused by the van der Waals force [37]. The morphology of the nanocomposite is irregularly granular and increases in size with the addition of CS, as shown in Figure 6(b). Similar particle sizes were also found in a study conducted by Sheikhmohammadi *et al.*, where CS–Fe_3O_4 nanocomposite had particle sizes ranging from 40.2 nm to 55.5 nm [38]. The increase in the particle size of the CS–Fe_3O_4/AC/TiO_2 nanocomposite is due to a thicker CS matrix, leading to a larger particle size in the nanocomposite. Further, Figure 6(c) shows that the CS–Fe_3O_4/AC/TiO_2 nanocomposite were successfully built due to the detection of the Ti and O that represent TiO_2 nanoparticles [39]. Meanwhile, the Fe and O represent Fe_3O_4 nanoparticles, and the C represents CS [32,33] and AC [40]. In addition, Au was also detected in the nanocomposites from the gold plating on the samples before testing [41]. Si was also detected in the nanocomposite, derived from the iron sand while preparing the Fe_3O_4 nanoparticles.

3.3 The functional groups of the CS–Fe_3O_4/AC/TiO_2 nanocomposite

The results of the FTIR characterization of the CS–Fe_3O_4/AC/TiO_2 nanocomposite are pictured in Figure 7. The Fe–OO and Fe–OT functional groups are located at wavenumbers 559.36 cm^{-1} to 569 cm^{-1} and 603 cm^{-1} to 610 cm^{-1}, respectively [27,31,38,42], where the appearance of these functional groups confirms that Fe_3O_4 nanoparticles have been successfully synthesized. Additionally, the Ti–O–Ti functional group was also detected at 713 cm^{-1}, which corresponds to the vibration of the Ti–O–Ti functional group [14]. At 926 cm^{-1} there is an N–H functional group which indicates the presence of CS [43]. At 1020 cm^{-1} to 1057 cm^{-1} , the C–O functional group was detected from AC [26,44]. In addition, the C–O functional group was also detected at 1176 cm^{-1} to 1183 cm^{-1} which is associated with the strain of the C–O group in the CS material [43]. The characteristics of CS were also indicated by the C–H functional group at 1338 cm^{-1} and the N–H functional group at 1609 cm^{-1} [38,42]. Moreover, the addition of CS in CFAT 2 to CFAT 5 introduced the C–N functional group at 1455 cm^{-1} to 1330 cm^{-1} [45]. Then, there is the C=C functional group at 1573 cm^{-1} and the C=O functional group at 1091 cm^{-1} to 1099 cm^{-1} and 2310 cm^{-1} to 2318 cm^{-1}, which are the characteristics of AC [42,43]. Additionally, at 3052 cm^{-1} to 3604 cm^{-1} and 3089 cm^{-1} to 3601 cm^{-1}, there is the stretching vibration of the aliphatic O–H and the stretching of the N–H from the $–NH_2$ group, respectively, which is characteristics of primary amines [46,47]. This occurs due to the presence of N–H groups and the complex intermolecular hydrogen bonding of the polysaccharide [48].

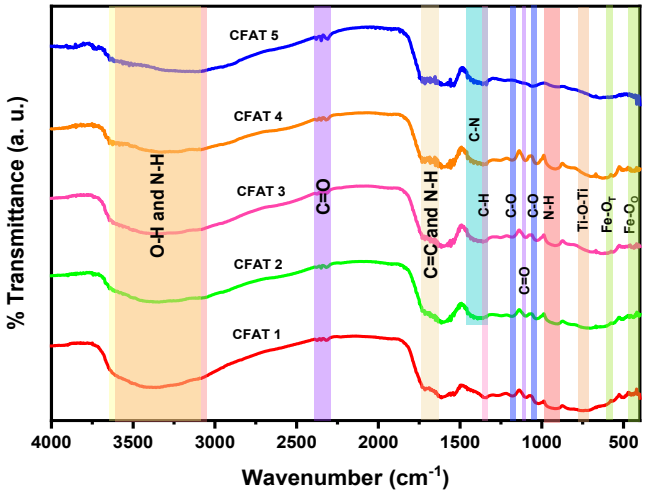

Figure 7. Functional groups of CFAT 1, CFAT 2, CFAT 3, CFAT 4, and CFAT 5.

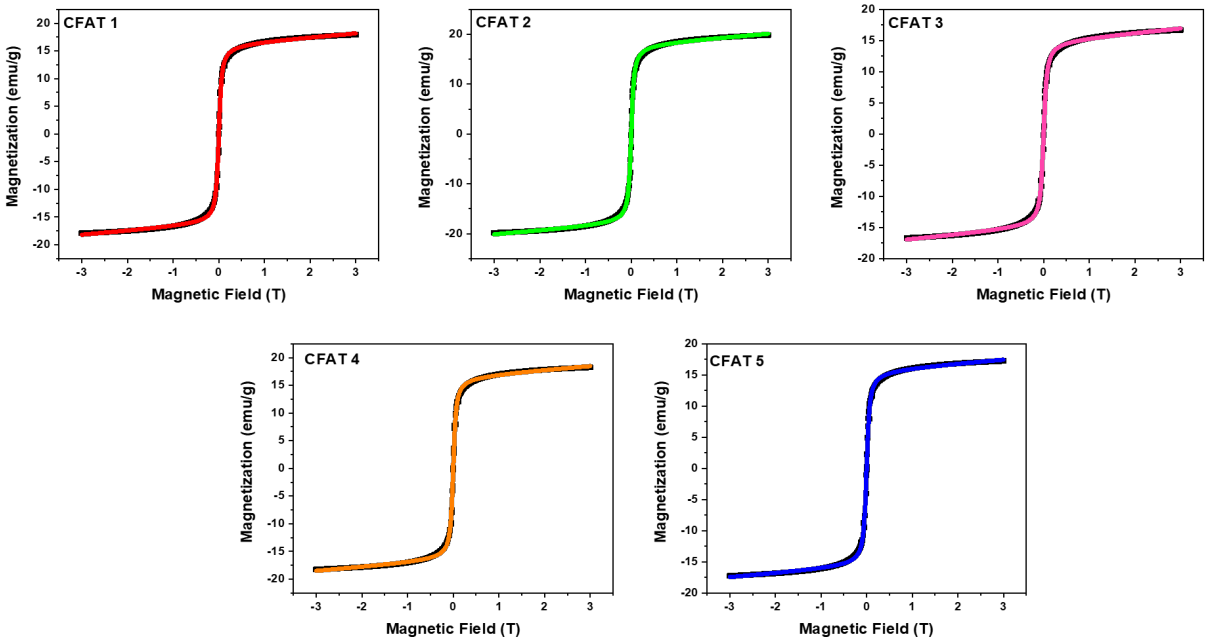

Figure 8. Hysteresis curves of CFAT 1, CFAT 2, CFAT 3, CFAT 4, and CFAT 5.

3.4 Magnetic properties of the CS–Fe_3O_4/AC/TiO_2 nanocomposite

The hysteresis curves of the CS–Fe_3O_4/AC/TiO_2 nanocomposite, analyzed using the Langevin model according to Equation (3) and Equation (4), are shown in Figure 8.

$$M = M_r + M_s \times \left(\coth(C \times H) - \frac{1}{C \times H}\right) + \chi \times H \quad (3)$$

$$C = \frac{\mu}{k_B T} \quad (4)$$

where M, M_r, and M_s are respectively magnetization, remanent magnetization and saturation magnetization (emu·g^{-1}), H is the magnetic field (T), χ is susceptibility, μ is permeability, k_B is the Boltzmann constant, and T refers to the temperature (K) [49]. The results are described in Table 1. Table 1 indicates that the remanent magnetization value ranges from 0.002 emu·g^{-1} to 0.014 emu·g^{-1}, and the coercive field ranges from 0.001 T to 0.011 T. These values are close to 0, so the hysteresis curves in Figure 8 resemble the letter S. These conditions indicate that the nanocomposites have superparamagnetism [50]. Furthermore, the saturation magnetization values tended to vary with the addition of CS mass, where the highest value was found in CFAT 2, which was 19.476 ± 0.025 emu·g^{-1}. This occurs because, based on EDX characterization, CFAT 2 has C content, which indicates the lowest CS and AC material compared to CFAT 1 and CFAT 3 to CFAT 5. CS and AC are non-magnetic materials, so that when the content of CS and AC in the sample is minimum, the saturation magnetization will have the greatest value [35].

Table 1. Magnetic parameters of CS–Fe_3O_4/AC/TiO_2 nanocomposite.

Sample	M_s [emu·g^{-1}]	M_r [emu·g^{-1}]	H_c [T]	χ
CFAT 1	17.577 ± 0.023	0.011 ± 0.010	0.001 ± 0.001	0.704 ± 0.013
CFAT 2	19.476 ± 0.025	0.014 ± 0.010	0.001 ± 0.001	0.756 ± 0.014
CFAT 3	16.372 ± 0.023	0.004 ± 0.018	0.004 ± 0.001	0.706 ± 0.012
CFAT 4	17.899 ± 0.023	0.012 ± 0.009	0.003 ± 0.001	0.688 ± 0.013
CFAT 5	16.950 ± 0.021	0.002 ± 0.001	0.011 ± 0.001	0.618 ± 0.012

Table 2. Parameters for the adsorption tests of Pb(II) heavy metal using CS–Fe_3O_4/AC/TiO_2 adsorbent.

Time [min]	Sample	Concentration Pb [ppm]		Solution volume [L]	Adsorbent mass [g]	Adsorption capacity (q_e) [mg·g^{-1}]	Efficiency [%]
		C_i	C_e				
30	CFAT 1	50.0 ± 0.5	0.6901 ± 0.1340	0.025 ± 0.013	0.05 ± 0.03	24.65 ± 0.07	98.62 ± 0.27
	CFAT 2	50.0 ± 0.5	2.2847 ± 0.2546	0.025 ± 0.013	0.05 ± 0.03	23.86 ± 0.13	95.43 ± 0.51
	CFAT 3	50.0 ± 0.5	1.1452 ± 0.0926	0.025 ± 0.013	0.05 ± 0.03	24.43 ± 0.05	97.71 ± 0.19
	CFAT 4	50.0 ± 0.5	1.1264 ± 0.1571	0.025 ± 0.013	0.05 ± 0.03	24.44 ± 0.08	97.75 ± 0.31
	CFAT 5	50.0 ± 0.5	0.9301 ± 0.1277	0.025 ± 0.013	0.05 ± 0.03	24.53 ± 0.06	98.14 ± 0.26
	CS	50.0 ± 0.5	3.8357 ± 0.0926	0.025 ± 0.013	0.05 ± 0.03	23.08 ± 0.14	92.33 ± 0.57
60	CFAT 1	50.0 ± 0.5	0.0865 ± 0.1340	0.025 ± 0.013	0.05 ± 0.03	24.96 ± 0.07	99.83 ± 0.27
	CFAT 2	50.0 ± 0.5	1.3932 ± 0.2546	0.025 ± 0.013	0.05 ± 0.03	24.30 ± 0.13	97.21 ± 0.51
	CFAT 3	50.0 ± 0.5	0.7748 ± 0.0926	0.025 ± 0.013	0.05 ± 0.03	24.61 ± 0.05	98.45 ± 0.19
	CFAT 4	50.0 ± 0.5	0.3903 ± 0.1571	0.025 ± 0.013	0.05 ± 0.03	24.81 ± 0.08	99.22 ± 0.31
	CFAT 5	50.0 ± 0.5	0.3765 ± 0.1277	0.025 ± 0.013	0.05 ± 0.03	24.80 ± 0.06	99.25 ± 0.26
	CS	50.0 ± 0.5	3.1966 ± 0.0926	0.025 ± 0.013	0.05 ± 0.03	23.40 ± 0.14	93.61 ± 0.57
90	CFAT 1	50.0 ± 0.5	0.1186 ± 0.1340	0.025 ± 0.013	0.05 ± 0.03	24.94 ± 0.07	99.76 ± 0.27
	CFAT 2	50.0 ± 0.5	0.9457 ± 0.2546	0.025 ± 0.013	0.05 ± 0.03	24.53 ± 0.13	98.11 ± 0.51
	CFAT 3	50.0 ± 0.5	0.8648 ± 0.0926	0.025 ± 0.013	0.05 ± 0.03	24.57 ± 0.05	98.27 ± 0.19
	CFAT 4	50.0 ± 0.5	0.3888 ± 0.1571	0.025 ± 0.013	0.05 ± 0.03	24.81 ± 0.08	99.22 ± 0.31
	CFAT 5	50.0 ± 0.5	0.2952 ± 0.1277	0.025 ± 0.013	0.05 ± 0.03	24.85 ± 0.06	99.41 ± 0.26
	CS	50.0 ± 0.5	2.4847 ± 0.0926	0.025 ± 0.013	0.05 ± 0.03	23.76 ± 0.14	95.03 ± 0.57
120	CFAT 1	50.0 ± 0.5	0.0620 ± 0.1340	0.025 ± 0.013	0.05 ± 0.03	24.97 ± 0.07	99.88 ± 0.27
	CFAT 2	50.0 ± 0.5	1.2402 ± 0.2546	0.025 ± 0.013	0.05 ± 0.03	24.38 ± 0.13	97.52 ± 0.51
	CFAT 3	50.0 ± 0.5	0.7300 ± 0.0926	0.025 ± 0.013	0.05 ± 0.03	24.64 ± 0.05	98.54 ± 0.19
	CFAT 4	50.0 ± 0.5	0.4908 ± 0.1571	0.025 ± 0.013	0.05 ± 0.03	24.75 ± 0.08	99.02 ± 0.31
	CFAT 5	50.0 ± 0.5	0.1596 ± 0.1277	0.025 ± 0.013	0.05 ± 0.03	24.92 ± 0.06	99.68 ± 0.26
	CS	50.0 ± 0.5	2.7375 ± 0.0926	0.025 ± 0.013	0.05 ± 0.03	23.63 ± 0.14	94.53 ± 0.57
150	CFAT 1	50.0 ± 0.5	0.1033 ± 0.1340	0.025 ± 0.013	0.05 ± 0.03	24.95 ± 0.07	99.79 ± 0.27
	CFAT 2	50.0 ± 0.5	1.2422 ± 0.2546	0.025 ± 0.013	0.05 ± 0.03	24.38 ± 0.13	97.52 ± 0.51
	CFAT 3	50.0 ± 0.5	0.6757 ± 0.0926	0.025 ± 0.013	0.05 ± 0.03	24.66 ± 0.05	98.65 ± 0.19
	CFAT 4	50.0 ± 0.5	0.4755 ± 0.1571	0.025 ± 0.013	0.05 ± 0.03	24.76 ± 0.08	99.05 ± 0.31
	CFAT 5	50.0 ± 0.5	0.3831 ± 0.1277	0.025 ± 0.013	0.05 ± 0.03	24.81 ± 0.06	99.23 ± 0.26
	CS	50.0 ± 0.5	2.5353 ± 0.0926	0.025 ± 0.013	0.05 ± 0.03	23.73 ± 0.14	94.93 ± 0.57

3.5 Pb(II) adsorption performance of the CS–Fe_3O_4/AC/TiO_2 nanocomposite

The adsorbent effectiveness of the CS–Fe_3O_4/AC/TiO_2 nanoparticles for Pb(II) heavy metal ions was assessed using an AAS instrument. The tests were conducted with contact times of 30 min, 60 min, 90 min, 120 min, and 150 min. Pure CS was also tested as a comparison to show the synergistic effect in CS–Fe_3O_4/AC/TiO_2 adsorbent and confirm the role of CS as a supporting matrix and adsorption capacity improver. The results show that the adsorption efficiency increases with the contact time. This is due to the large number of adsorption sites on the sample, where the absorption process continues to increase until saturation [2]. The data from the tests and the parameters used are presented in Table 2 and Figure 9. In CFAT 2 to CFAT 5, the adsorbed Pb concentration increased with the addition of CS mass, resulting in a higher efficiency percentage. Sample CFAT 1 achieved the highest efficiency value (99.88%) at a contact time of 120 min, while the lowest efficiency value (92.33%) was obtained from pure CS at a contact time of 30 min. Sample CFAT 5, with the highest CS mass (1.00 g), reached the efficiency value of 99.68% at 120 min of contact time. Among the samples containing CS, sample CFAT 2 had the lowest efficiency value of 93.97% in 30 min of contact time.

Table 2 indicates that CFAT 1 has a higher adsorption capacity for Pb than samples CFAT 2 to CFAT 5, although samples CFAT 2 to CFAT 5 exhibit better performance than pure CS. Based on Table 2, it is known that the largest adsorption capacity of pure CS is 23.73 $mg{\cdot}g^{-1}$ while CFAT 1 to CFAT 5 has an adsorption capacity between 23.86 $mg{\cdot}g^{-1}$ and 24.97 $mg{\cdot}g^{-1}$. These results indicate that CFAT 1 to CFAT 5 has better adsorption ability compared to CS. Furthermore, previous research on $Mg_{0.2}Fe_{2.8}O_4$/AC/TiO_2 composites as Pb(II) heavy metal adsorbents showed an adsorbing capacity of 22.38 $mg{\cdot}g^{-1}$ [22]. This adsorption capacity is not higher than the CFAT 1 to CFAT 5 adsorbents in this study. This shows a good synergy between CS and Fe_3O_4/AC/TiO_2 nanocomposite as an adsorbent for Pb(II) heavy metal.

Based on Figure 9, CFAT 1 started to show a slight decrease in efficiency at 90 min absorption time, while CFAT 5 at 90 min still showed an increase in efficiency. This is due to the presence of functional chemical groups in CS, which causes its adsorption performance to be more stable in CFAT 5. Furthermore, Table 2 shows that CFAT 1 has a greater adsorption capacity compared to CFAT 2 to CFAT 5. This is due to CFAT 1 having more OH functional groups than CFAT 2 to CFAT 5, thus CFAT 1 is able to adsorb more Pb(II). This result is confirmed by FTIR characterization, which shows that CFAT 1 exhibits an OH absorption peak with greater intensity compared to CFAT 2 to CFAT 5. Furthermore, the SEM characterization results show that CFAT 1 sample has the smallest particle size. The smaller particle size will cause the surface area of the sample to be larger, so that the greater the ability of the sample to absorb heavy metal Pb(II) [51]. This is causing the absorption capacity of CFAT 1 to have the largest value.

The process of Pb(II) adsorption by the CS–Fe_3O_4/AC/TiO_2 adsorbent involves three distinct steps. The first step is external diffusion, where Pb(II) in the wastewater moves through the liquid layer surrounding the CS–Fe_3O_4/AC/TiO_2 adsorbent. The concentration gradient between the Pb(II) solution and the adsorbent surface serves as the driving force for the external diffusion. The second step is internal diffusion, where Pb(II) diffuses into the pores of the CS–Fe_3O_4/AC/TiO_2 adsorbent. The third step involves the adsorption of the Pb(II) adsorbate at the active sites of the CS–Fe_3O_4/AC/TiO_2 adsorbent. This process involves electrostatic interactions between the functional chemical groups of CS and Pb(II) [25,52]. This adsorption mechanism is shown in Figure 10.

Based on Figure 11, adsorption starts rapidly during the first 30 min of the reaction and then slows and finally reaches a state of equilibrium (plateau). As seen in Figure 11, the adsorption process appears stable from a contact time of 60 min to 150 min. This phenomenon indicates that there are still many active sites at the start of absorption and they will decrease over a certain time. Therefore, at longer contact times, the molecules require additional time to diffuse into the pores of the adsorbent [53]. These are the characteristics of the Pseudo-first-order (PFO) kinetic model. Furthermore, Table 3 shows a comparison of the values of the Pseudo-first-order (PFO) and Pseudo-second-order (PSO) kinetic models. The analysis shows that the PFO model has the highest coefficient of determination (R_2) value of 1.000 with an equilibrium adsorption capacity (q_e) of 24.955 $mg{\cdot}g^{-1}$. An R_2 value close to 1 indicates that the PFO model fits the experimental data. Therefore, the PFO model is the most suitable and accurate overall in explaining the adsorption of Pb(II) heavy metal.

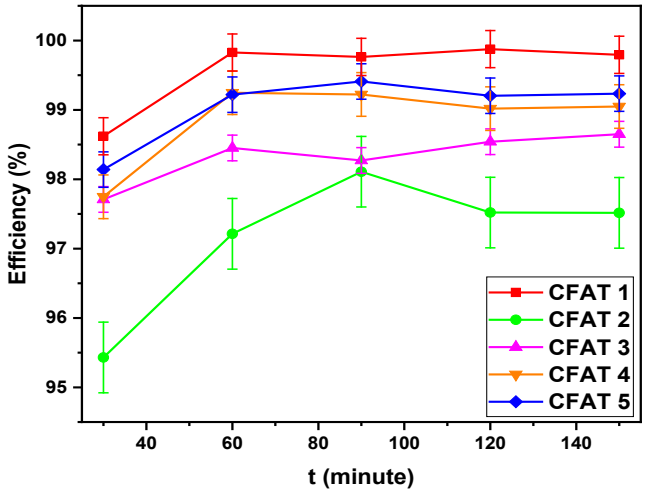

Figure 9. Adsorption efficiency of Pb(II) heavy metal versus the contact time of CFAT 1, CFAT 2, CFAT 3, CFAT 4, and CFAT 5.

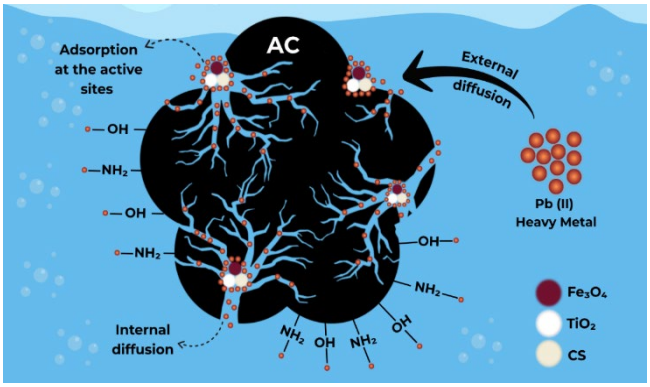

Figure 10. Adsorption mechanism of CS–Fe_3O_4/AC/TiO_2 on Pb(II) heavy metal.

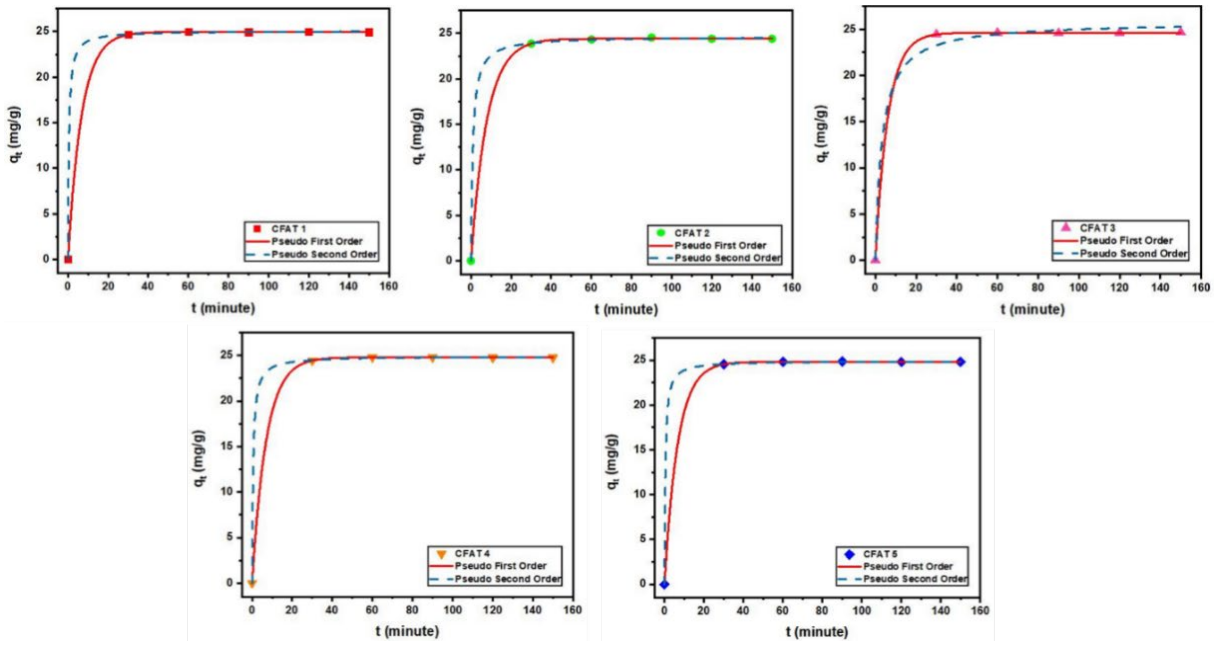

Figure 11. Graphic of the PFO and PSO kinetic model of CFAT 1, CFAT 2, CFAT 3, CFAT 4, and CFAT 5.

Table 3. Parameters of the PFO and PSO kinetic modeling.

Sample	Pseudo first-order			Pseudo second-order		
	q_e [mg·g^{-1}]	K_1 [menit^1]	R^2	q_e [mg·g^{-1}]	K_2 [g·mg^{-1}·min^{-1}]	R^2
CFAT 1	24.955 ± 0.106	0.147 ± 0.006	1.000	25.071 ± 0.221	0.085 ± 0.016	0.999
CFAT 2	24.401 ± 0.106	0.127 ± 0.006	0.999	24.625 ± 0.221	0.044 ± 0.016	0.999
CFAT 3	24.620 ± 0.106	0.162 ± 0.006	0.999	25.804 ± 0.221	0.012 ± 0.016	0.945
CFAT 4	24.783 ± 0.106	0.142 ± 0.006	1.000	24.908 ± 0.221	0.077 ± 0.016	0.999
CFAT 5	24.819 ± 0.106	0.149 ± 0.006	1.000	24.928 ± 0.221	0.091 ± 0.016	0.999

Table 4. Test results for Pb (II) heavy metal adsorption using CS-Fe_3O_4/AC/TiO_2 adsorbent.

Cycle	Sample	Concentration Pb [ppm]		Solution volume	Adsorbent mass	Adsorption capacity (q_e)	Efficiency
		C_i	C_e	[L]	[g]	[mg·g^{-1}]	[%]
1	CFAT 1	50.0 ± 0.5	0.8814 ± 0.7851	0.025 ± 0.013	0.05 ± 0.03	24.56 ± 0.39	98.24 ± 1.57
	CFAT 2	50.0 ± 0.5	3.8411 ± 0.7851	0.025 ± 0.013	0.05 ± 0.03	23.08 ± 0.39	92.32 ± 1.57
	CFAT 3	50.0 ± 0.5	2.4153 ± 0.7851	0.025 ± 0.013	0.05 ± 0.03	23.79 ± 0.39	95.17 ± 1.57
	CFAT 4	50.0 ± 0.5	0.1960 ± 0.7851	0.025 ± 0.013	0.05 ± 0.03	24.90 ± 0.39	99.61 ± 1.57
	CFAT 5	50.0 ± 0.5	0.2907 ± 0.7851	0.025 ± 0.013	0.05 ± 0.03	24.85 ± 0.39	99.42 ± 1.57
2	CFAT 1	50.0 ± 0.5	0.8229 ± 0.1780	0.025 ± 0.013	0.05 ± 0.03	24.59 ± 0.09	98.35 ± 0.36
	CFAT 2	50.0 ± 0.5	1.0627 ± 0.1780	0.025 ± 0.013	0.05 ± 0.03	24.47 ± 0.09	97.87 ± 0.36
	CFAT 3	50.0 ± 0.5	0.7465 ± 0.1780	0.025 ± 0.013	0.05 ± 0.03	24.63 ± 0.09	98.51 ± 0.36
	CFAT 4	50.0 ± 0.5	0.3159 ± 0.1780	0.025 ± 0.013	0.05 ± 0.03	24.84 ± 0.09	99.37 ± 0.36
	CFAT 5	50.0 ± 0.5	0.2176 ± 0.1780	0.025 ± 0.013	0.05 ± 0.03	24.89 ± 0.09	99.56 ± 0.36
3	CFAT 1	50.0 ± 0.5	0.8831 ± 0.1659	0.025 ± 0.013	0.05 ± 0.03	24.56 ± 0.08	98.23 ± 0.33
	CFAT 2	50.0 ± 0.5	1.2738 ± 0.1659	0.025 ± 0.013	0.05 ± 0.03	24.36 ± 0.08	97.45 ± 0.33
	CFAT 3	50.0 ± 0.5	0.7164 ± 0.1659	0.025 ± 0.013	0.05 ± 0.03	24.64 ± 0.08	98.57 ± 0.33
	CFAT 4	50.0 ± 0.5	0.4731 ± 0.1659	0.025 ± 0.013	0.05 ± 0.03	24.76 ± 0.08	99.05 ± 0.33
	CFAT 5	50.0 ± 0.5	0.4819 ± 0.1659	0.025 ± 0.013	0.05 ± 0.03	24.76 ± 0.08	99.04 ± 0.33
4	CFAT 1	50.0 ± 0.5	0.7695 ± 0.1795	0.025 ± 0.013	0.05 ± 0.03	24.62 ± 0.09	98.46 ± 0.36
	CFAT 2	50.0 ± 0.5	1.1196 ± 0.1795	0.025 ± 0.013	0.05 ± 0.03	24.44 ± 0.09	97.76 ± 0.36
	CFAT 3	50.0 ± 0.5	0.7983 ± 0.1795	0.025 ± 0.013	0.05 ± 0.03	24.60 ± 0.09	98.40 ± 0.36
	CFAT 4	50.0 ± 0.5	0.2415 ± 0.1795	0.025 ± 0.013	0.05 ± 0.03	24.88 ± 0.09	99.52 ± 0.36
	CFAT 5	50.0 ± 0.5	0.3471 ± 0.1795	0.025 ± 0.013	0.05 ± 0.03	24.83 ± 0.09	99.31 ± 0.36
5	CFAT 1	50.0 ± 0.5	6.7631 ± 0.8241	0.025 ± 0.013	0.05 ± 0.03	24.83 ± 0.08	86.47 ± 1.65
	CFAT 2	50.0 ± 0.5	6.4445 ± 0.8241	0.025 ± 0.013	0.05 ± 0.03	21.62 ± 0.08	87.11 ± 1.65
	CFAT 3	50.0 ± 0.5	5.0633 ± 0.8241	0.025 ± 0.013	0.05 ± 0.03	21.78 ± 0.08	89.87 ± 1.65
	CFAT 4	50.0 ± 0.5	3.3821 ± 0.8241	0.025 ± 0.013	0.05 ± 0.03	22.47 ± 0.08	93.24 ± 1.65
	CFAT 5	50.0 ± 0.5	3.2530 ± 0.8241	0.025 ± 0.013	0.05 ± 0.03	23.31 ± 0.08	93.49 ± 1.65

Table 5. Comparison of several adsorbents absorbing Pb(II) heavy metal.

Adsorbent	Adsorbent mass [g]	q_e [mg·g^{-1}]	Kinetic	Recycle conditions	Ref.
Magnetic bioadsorbent based on carbon quantum dots (Fe_3O_4–PPCQDs) from *Pomegranate peel* (PP)	0.1	23.75	N/A	N/A	[54]
Chitosan/iron oxide nanocomposite	0.05	3.795	PSO	N/A	[55]
Chitosan/poly(ethylene oxide) nanofibers	0.05	17.42	PSO	Desorption time: 12 h Temperature: 80°C Recycle number: 5	[56]
CFAT 1	0.05	24.95			
CFAT 2	0.05	24.38		Desorption time: 60 min	
CFAT 3	0.05	24.66	PFO	Temperature: room temperature	This work
CFAT 4	0.05	24.76		Recycle number: 5	
CFAT 5	0.05	24.81			

*N/A: information not available

This research also evaluates the adsorbent regeneration capability by conducting five-cycle adsorption-desorption tests on the CFAT 1 to CFAT 5 samples. The samples used for Pb (II) adsorption at a contact time of 120 min were washed with 0.1 M HCl for 60 min under constant stirring at room temperature. Next, it was centrifuged to obtain the precipitate and then washed again with distilled water until the pH was neutral. After desorption, samples CFAT 1 to CFAT 5 were reused for adsorption with the same solution volume (0.025 L) and contact time (120 min). This process is repeated until the adsorbent's performance is no longer effective, as evident from the C_e concentration in the fifth cycle, which remains high after the adsorption process, decreasing from 3.2530 ppm to 6.7631 ppm compared to the previous cycle. The AAS characterization results from the five adsorption-desorption cycles are presented in Table 4. The results show that the CS–Fe_3O_4/AC/TiO_2 adsorbent maintains its adsorption efficiency, although a slight decrease in efficiency was observed in cycle 1 to cycle 4; however, there was a significant decrease in cycle 5. This indicates that CFAT 1 to CFAT 5 samples can be reused after regeneration [57] with stability comparable to that of up to 4 repetitions.

The adsorbing capacity of the CS–Fe_3O_4/AC/TiO_2 adsorbent as Pb(II) heavy metal adsorbent compared with other adsorbents is summarized in Table 5. Based on Table 5, the adsorbing capacity of CFAT adsorbents 1 to 5 showed good values of 24.95 mg·g^{-1}, 24.38 mg·g^{-1}, 24.66 mg·g^{-1}, 24.76 mg·g^{-1}, and 24.81 mg·g^{-1} respectively compared to other adsorbents which had adsorbing capacities below 20 mg·g^{-1} for the same adsorbent mass [55,56]. Interestingly, the adsorption capacity of CFAT adsorbents 1 to 5 remains higher than that of magnetic bioadsorbent based on carbon quantum dots (Fe_3O_4–PPCQDs) from Pomegranate peel (PP) which has twice the adsorbent mass [54]. Furthermore, CFAT adsorbents 1 to 5 are capable of repeated use at room temperature and relatively low desorption time compared to chitosan/poly(ethylene oxide) nanofibers adsorbent [56]. This shows that CFAT adsorbents 1 to 5 are promising materials as Pb(II) heavy metal adsorbents because they have good adsorption capacity and can be used repeatedly.

4. Conclusions

The CS-Fe_3O_4/AC/TiO_2 nanocomposite were successfully synthesized using the coprecipitation method to produce Fe_3O_4 and TiO_2, the carbonization method to produce AC, and the ex-situ method to produce CS-Fe_3O_4/AC/TiO_2 nanocomposite. The characterization results show that the crystallite size of Fe_3O_4 is 16.1 nm to 24.5 nm with a cubic spinel phase, while the crystallite size of TiO_2 is 25.2 nm with a rutile phase. The morphology of the CS-Fe_3O_4/AC/TiO_2 particles is irregularly spherical and shows aggregation, with a particle size distribution of 31.4 nm to 48.0 nm. Furthermore, the presences of N–H, Fe–O, C=O, and Ti–O–Ti functional groups, which are characteristics of CS, Fe_3O_4, AC, and TiO_2, indicate that the CS-Fe_3O_4/AC/TiO_2 nanocomposite was successfully synthesized. The CS-Fe_3O_4/AC/TiO_2 nanocomposite exhibited superparamagnetic properties, as indicated by its coercivity and remnant magnetization values being close to zero. The addition of CS mass resulted in high-efficiency percentages, reaching 99.68% for CFAT 5 and 99.88% for CFAT 1. Additionally, the CS-Fe_3O_4/AC/TiO_2 adsorbent can be reused with optimal performance for four adsorption-desorption cycles. Based on the results obtained, the CS–Fe_3O_4/AC/TiO_2 nano composite with natural precursors has good potential to be applied as an adsorbent for the heavy metal Pb(II) in industrial wastewater treatment.

Acknowledgements

This research was funded by Universitas Negeri Malang through the "Penelitian Unggulan Pusat" scheme with contract number 4.4.555/UN32.14.1/LT/2024.

References

[1] P. Higgins, R. Kumar, and S. H. Siddiqui, "Synthesis and characterization of SiO_2/GO/Al_2O_3 nanocomposite adsorbent for the uptake of ciprofloxacin: Isothermal and reusability studies," *Journal of the Iranian Chemical Society*, vol. 22, no. 2, pp. 407–418, 2025.

[2] M. S. Rostami, and M. M. Khodaei, "Recent advances in chitosan-based nanocomposites for adsorption and removal of heavy metal ions," *International Journal of Biological Macromolecules*, vol. 270, p. 132386, 2024.

[3] Y. B. Nthwane, B. G. Fouda-Mbanga, M. Thwala, and K. Pillay, "A comprehensive review of heavy metals (Pb^{2+}, Cd^{2+}, Ni^{2+}) removal from wastewater using low-cost adsorbents and possible revalorisation of spent adsorbents in blood fingerprint application," *Environmental Technology*, vol. 46, no. 3, pp. 414–430, 2025.

[4] T. Shaikh, "Adsorption of Pb(II) from wastewater by natural and synthetic adsorbents," *Biointerface Research in Applied Chemistry*, vol. 10, no. 5, pp. 6522–6539, 2020.

[5] S. Mohammadi, A. Kosari, H. Eslami, E. F. Moghadam, and A. Ghaffarian-Bahraman, "Toxic metal contamination in edible salts and its attributed human health risks: A systematic review and meta-analysis," *Environmental Science and Pollution Research,* vol. 32, no. 7, pp. 4313–4324, 2025.

[6] B. Kayranli, O. Gök, T. Yilmaz, G. Gok, H. Çelebi, I. Y. Seçkin, and Ö. Ç. Mesutoğlu, "Low-cost organic adsorbent usage for removing Ni^{2+} and Pb^{2+} from aqueous solution and adsorption mechanisms," *International Journal of Environmental Science and Technology*, vol. 19, no. 5, pp. 3547–3564, 2022.

[7] N. Abd-Talib, C. S. Chuong, S. H. Mohd-Setapar, U. A. Asli, K. F. Pa'ee, and K. Y. T. Len, "Trends in adsorption mechanisms of fruit peel adsorbents to remove wastewater pollutants (Cu(II), Cd(II) and Pb(II))," *Journal of Water and Environment Technology*, vol. 18, no. 5, pp. 290–313, 2020.

[8] K. Raj, and A. P. Das, "Lead pollution: Impact on environment and human health and approach for a sustainable solution," *Environmental Chemistry and Ecotoxicology*, vol. 5, pp. 79–85, 2023.

[9] E. S. Soedjono, A. Slamet, N. Fitriani, M. S. Sumarlan, A. Supriyanto, D. R. M. Isnadina, and N. B. Othman, "Residual seawater from salt production (bittern) as a coagulant to remove lead (Pb^{2+}) and turbidity from batik industry wastewater," *Heliyon*, vol. 7, no. 11, p. e08268, 2021.

[10] J. R. Miller, J. P. Gannon, and K. Corcoran, "Concentrations, mobility, and potential ecological risks of selected metals within compost amended, reclaimed coal mine soils, tropical South Sumatra, Indonesia," *AIMS Environmental Science*, vol. 6, no. 4, pp. 298–325, 2019.

[11] L. Setyaningsih, F. Azhar Dikdayatama, and A. S. Wulandari, "Arbuscular mycorrhizal fungi and rhizobium enhance the growth of samanea saman (trembesi) planted on gold-mine tailings in Pongkor, West Java, Indonesia," *Biodiversitas, Journal of Biological Diversity*, vol. 21, no. 2, 2020.

[12] G. K. Kinuthia, V. Ngure, D. Beti, R. Lugalia, A. Wangila, and L. Kamau, "Levels of heavy metals in wastewater and soil samples from open drainage channels in Nairobi, Kenya: Community health implication," *Scientific Reports*, vol. 10, no. 1, p. 8434, 2020.

[13] A. A. Sabrin A, 'Textile dye removal from wastewater effluents using chitosan-ZnO nanocomposite," *Journal of Textile Science and Engineering*, vol. 05, no. 03, pp. 5–8, 2015.

[14] H. Yousefzadeh, A. A. Salarian, and H. Sid Kalal, "Study of Pb(II) adsorption from aqueous solutions by TiO_2 functionalized with hydroxide ethyl aniline (PHEA/n-TiO_2)," *Journal of Molecular Liquids*, vol. 263, pp. 294–302, 2018.

[15] Q. Guo, C. Zhou, Z. Ma, and X. Yang, "Fundamentals of TiO_2 photocatalysis: Concepts, mechanisms, and challenges," *Advanced Materials*, vol. 31, no. 50, pp. 1–26, 2019.

[16] J. F. Jeevakumari, and G. Suresh, "Comprehensive evaluation of solvothermally synthesized Fe_3O_4 and PEG capped Fe_3O_4 nanoparticles for magnetic and biomedical applications," *Inorganic Chemistry Communications*, vol. 174, p. 113904, 2025.

[17] K. Kalantari, M. B. Ahmad, H. R. F. Masoumi, K. Shameli, M. Basri, and R. Khandanlou, "Rapid adsorption of heavy metals by Fe_3O_4/talc nanocomposite and optimization study using response surface methodology," *International Journal of Molecular*, vol. 15, no. 7, pp. 12913–12927, 2014.

[18] H. Zhan, Y. Bian, Q. Yuan, B. Ren, A. Hursthouse, and G. Zhu, "Preparation and potential applications of superparamagnetic Nano-Fe_3O_4," *Processes*, vol. 6, no. 4, pp. 1–22, 2018.

[19] D. Sartika, E. Malis, E. S. Mangunang, "Analisis distribusi nano-partikel Fe_3O_4 terhadap penyerapan logam berat Pb," *Journal Teknologi Technoscientia*, vol. 12 No.1, no. 1, pp. 8–11, 2019.

[20] S. Jafari, F. Zhao, D. Zhao, M. Lahtinen, A. Bhatnagar, and M. Sillanpää, "A comparative study for the removal of methylene blue dye by N and S modified TiO_2 adsorbents," *Journal of Molecular Liquids*, vol. 207, pp. 90–98, 2015.

[21] E. Asuquo, A. Martin, P. Nzerem, F. Siperstein, and X. Fan, "Adsorption of Cd(II) and Pb(II) ions from aqueous solutions using mesoporous activated carbon adsorbent: Equilibrium, kinetics and characterisation studies," *Journal of Environmental Chemical Engineering*, vol. 5, no. 1, pp. 679–698, 2017.

[22] B. W. Putri, A. Taufiq, C. I. Yogihati, S. T. U. I. Subadra, Sunaryono, N. Mufti, M. Diantoro, and M. S. A. Aziz, "Synthesis of nano-sized $Mg_{0.2}Fe_{2.8}O_4$/AC/TiO_2 composite for removal Pb(II) from water," *AIP Conference Proceedings*, vol. 3068, no. 1, p. 040005, 2024.

[23] I. Aranaz, A. Alcántara, M. C. Civera, C. Arias, B. Elorza, A. Heras, and F. N. A. Contreras, "Chitosan: An overview of its properties and applications," *Polymers*, vol. 13, no. 19, p. 3256, 2021.

[24] F. G. L. M. Borsagli, and A. Borsagli, "Chemically modified chitosan bio-sorbents for the competitive complexation of heavy metals ions: A potential model for the treatment of wastewaters and industrial spills," *Journal of Polymers and the Environment*, vol. 27, no. 7, pp. 1542–1556, 2019.

[25] S. Begum, N. Y. Yuhana, N. Md Saleh, N. H. N. Kamarudin, and A. B. Sulong, "Review of chitosan composite as a heavy metal adsorbent: Material preparation and properties," *Carbohydrate Polymers*, vol. 259, p. 117613, 2021.

[26] E. H. Sujiono, D. Zabrian, Zurnansyah, M.ulyati, V. Zharvan, Samnur, and N. A. Humairah, "Fabrication and characterization of coconut shell activated carbon using variation chemical activation for wastewater treatment application," *Results in Chemistry*, vol. 4, p. 100291, 2022.

[27] A. Taufiq, R. E. Saputro, Sunaryono, N. Hidayat, A. Hidayat, N. Mufti, M. Diantoro, A. Patriati, Mujamilah, E. G. R. Putra, and H. Nur, "Fabrication of magnetite nanoparticles dispersed in olive oil and their structural and magnetic investigations," *IOP Conference Series Materials Science and Engineering*, vol. 202, no. 1, p. 012008, 2017.

[28] A. Taufiq, "Effects of the Annealing temperature on the structure evolution and antifungal performance of TiO_2/Fe_3O_4 nanocomposites manufactured from natural sand," *Nano*, vol. 16, no. 2, pp. 1–12, 2021.

[29] K. M. Dimpe, J. C. Ngila, and P. N. Nomngongo, "Application of waste tyre-based activated carbon for the removal of heavy

metals in wastewater," *Cogent Engineering*, vol. 4, no. 1, pp. 1–11, 2017.

[30] E. Abu-Danso, S. Peräniemi, T. Leiviskä, and A. Bhatnagar, "Synthesis of s-ligand tethered cellulose nanofibers for efficient removal of Pb(II) and Cd(II) ions from synthetic and industrial wastewater," *Environmental Pollution*, vol. 242, no. part B, pp. 1988–1997, 2018.

[31] A. Gholizadeh, "A comparative study of physical properties in Fe_3O_4 nanoparticles prepared by coprecipitation and citrate methods," *Journal of the American Ceramic Society*, vol. 100, no. 8, pp. 3577–3588, 2017.

[32] V. M. Vinosel, M. Asisi Janifer, S. Anand, and S. Pauline, "Structural and functional group characterization of nano-composite Fe_3O_4/TiO_2 and its magnetic property," *Mechanic, Materials Science & Engineering*, vol 9, no. 1, pp. 01499407, 2017.

[33] A. R. Liandi, A. H. Cahyana, R. T. Yunarti, and T. P. Wendari, "Facile synthesis of magnetic Fe_3O_4@chitosan nanocomposite as environmentally green catalyst in multicomponent Knoevenagel-Michael domino reaction," *Ceramics International*, vol. 48, no. 14, pp. 20266–20274, 2022.

[34] J. Ruey-Shin, Y. Yao-Chung, L. Chien-Shiun, L. Kuen-Song, L. His-Chuan, W. Sea-Fue, and S. An-Cheng, "Synthesis of magnetic Fe_3O_4/activated carbon nanocomposites with high surface area as recoverable adsorbents," *Journal of the Taiwan Institute of Chemical Engineers*, vol. 90, pp. 51–60, 2018.

[35] S. Afzal, N. M. Julkapli, and L. K. Mun, "Visible light active TiO_2/CS/Fe_3O_4 for nitrophenol degradation: Studying impact of TiO_2, CS and Fe_3O_4 loading on the optical and photocatalytic performance of nanocomposite," *Materials Science in Semi-conductor Processing*, vol. 131, no. March, p. 105891, 2021.

[36] I. O. Wulandari, D. J. D. H. Santjojo, R. A. Shobirin, and A. Sabarudin, "Characteristics and magnetic properties of chitosan-coated Fe_3O_4 nanoparticles prepared by ex-situ co-precipitation method," *RASĀYAN Journal of Chemistry*, vol. 10, no. 4, pp. 1348–1358, 2017.

[37] L. R. Herawati, A. Taufiq, H. Wisodo, N. Hidayat, and N. Mufti, "Antifungal activities of Fe_3O_4/Ag nanocomposites covered by diethylamine template," *AIP Conference Proceedings*,vol. 2748, p. 020035, 2023.

[38] A. Sheikhmohammadi, and J. Yeganeh, "Application of the Fe_3O_4-chitosan nano-adsorbent for the adsorption of metronidazole from wastewater : Optimization, kinetic, thermodynamic and equilibrium studies," vol. 164, pp. 694–706, 2020.

[39] N. Mufti, U. Munfarriha, A. Fuad, and M. Diantoro, "Synthesis and photocatalytic properties of Fe_3O_4@TiO_2 core-shell for degradation of Rhodamine B," *AIP Conference Proceedings*, vol. 1712, no. 1, p. 050009, 2016.

[40] J. C. Ríos-Hurtado, E. M. Múzquiz-Ramos, A. Zugasti-Cruz, and D. A. Cortés-Hernández, "Mechanosynthesis as a simple method to obtain a magnetic composite (activated carbon/Fe_3O_4) for hyperthermia treatment," *Journal of Biomaterials and Nano-biotechnology*, vol. 07, no. 01, pp. 19–28, 2016.

[41] S. N. Qoidah St. U. I. Subadra, A. Taufiq, N. Mufti, S. Sunaryono, N. Hidayat, E. Handoko, M. Alaydrus, and T. Amrillah, "Fe_3O_4/MWCNT/TiO_2 nanocomposites as excellent microwave absorber material," *Journal of Alloys and Compounds*, vol. 970, no. 1, p. 172590, 2024.

[42] M. Liu, X. Zhang, Z. Li, L. Qu, and R. Han, "Fabrication of zirconium(IV)-loaded chitosan/Fe_3O_4/graphene oxide for efficient removal of alizarin red from aqueous solution," *Carbohydrate Polymers*, vol. 248, no. May, p. 116792, 2020.

[43] J. K. Fatombi, "Adsorption of indigo carmine from aqueous solution by chitosan and chitosan/activated carbon composite: Kinetics, isotherms and thermodynamics studies," *Fibers and Polymers*, vol. 20, no. 9, pp. 1820–1832, 2019.

[44] M. A. Shaker, and A. A. Yakout, "Optimization, isotherm, kinetic and thermodynamic studies of Pb(II) ions adsorption onto n-maleated chitosan-immobilized tio2 nanoparticles from aqueous media," *Spectrochimica Acta Part A: Molecular and Biomolecular Spectroscopy*, vol. 154, pp. 145–156, 2016.

[45] L. Qi, Z. Xu, X. Jiang, C. Hu, and X. Zou, "Preparation and antibacterial activity of chitosan nanoparticles," *Carbohydrate Research*, vol. 339, no. 16, pp. 2693–2700, 2004.

[46] H. Choi, "Applicability of composite beads, spent coffee grounds/ chitosan, for the adsorptive removal of Pb(II) from aqueous solutions," vol. 30, no. 5, pp. 536–545, 2019.

[47] I. L. D. Wijayanti, and F. W. Mahatmanti, "Synthesis of chitosan/ activated carbon composite beads as an adsorbent of Pb(II) and Cu(II) ions in aqueous solution: A review," *Indonesian Journal of Chemical Science*, vol. 11, no. 2, pp. 190–197, 2022.

[48] S. R. Mousavi-Qeydari, A. Samimi, D. Mohebbi-Kalhori, and E. Ahmadi, "A mesoporous melamine/chitosan/activated carbon biocomposite: Preparation, characterization and and its its application for Ni(II) uptake via ion imprinting," *International Journal of Biological Macromolecules*, vol. 188, no. August, pp. 126–136, 2021.

[49] N. Hanifah, St. U. I. Subadra, N. Hidayat, Sunaryono, C. I. Yogihati, W.A. Adi, Munasir, .T Amrillah, M. S. A. Aziz, and A. Taufiq, "A novel Fe_3O_4/ZnO/PANI/rGO nanohybrid material for radar wave absorbing," *Materials Chemistry and Physics*, vol. 317, p. 129169, 2024.

[50] J. S. Lee, J. M. Cha, H. Y. Yoon, J. K. Lee, and Y. K. Kim, "Magnetic multi-granule nanoclusters: A model system that exhibits universal size effect of magnetic coercivity," *Scientific Reports*, vol. 5, no. January, pp. 1–7, 2015.

[51] L. Hou, Q. Liang, and F. Wang, "Mechanisms that control the adsorption–desorption behavior of phosphate on magnetite nanoparticles: The role of particle size and surface chemistry characteristics," *RSC Advances*, vol. 10, no. 4, pp. 2378–2388, 2020.

[52] J. Wang, and X. Guo, "Adsorption kinetic models: Physical meanings, applications, and solving methods," *Journal of Hazardous Materials*, vol. 390, p. 122156, 2020.

[53] Y. Raji, A. Nadi, M. Rouway, S. J. Sbai, W. Yassine, A. Elmahbouby, O. Cherkaoui, and S. Zyade, "Efficient adsorption of methyl orange on nanoporous carbon from agricultural wastes: Characterization, kinetics, thermodynamics, regeneration and adsorption mechanism," *Journal of Composites Science*, vol. 6, no. 12, p. 385, 2022.

[54] H. Asadollahzadeh, M. Ghazizadeh, and M. Manzari, "Developing a magnetic nanocomposite adsorbent based on carbon quantum dots prepared from Pomegranate peel for the removal of Pb(II) and Cd(II) ions from aqueous solution," *Analytical Methods in Environmental Chemistry Journal*, vol. 4, no. 3, pp. 33–46, 2021.

[55] M. Keshvardoostchokami, L. Babaei, A. A. Zamani, A. H. Parizanganeh, and F. Piri, "Synthesized chitosan/iron oxide nanocomposite and shrimp shell in removal of nickel, cadmium and lead from aqueous solution," *Global Journal of Environmental Science and Management*, vol. 3, no. 3, pp. 267–278, 2017.

[56] M. I. Shariful, S. B. Sharif, J. J. L. Lee, U. Habiba, B. C. Ang, and M. A. Amalina, "Adsorption of divalent heavy metal ion by mesoporous-high surface area chitosan/poly (ethylene oxide) nanofibrous membrane," *Carbohydrate Polymers*, vol. 157, pp. 57–64, 2017.

[57] T. N. Dharmapriya, D. Li, Y.-C. Chung, and P.-J. Huang, "Green synthesis of reusable adsorbents for the removal of heavy metal ions," *ACS Omega*, vol. 6, no. 45, pp. 30478–30487, 2021.